

Automated shaker placement and regularized input estimation for MIMO testing

Keaton Coletti ^{*1,2}, R. Benjamin Davis ^{†1}, and Ryan Schultz ^{‡2}

¹College of Engineering, University of Georgia, 30602, Athens, Georgia, United States

²Sandia National Laboratories, Albuquerque, 87123, New Mexico, United States

Abstract

Multi-input, multi-output (MIMO) testing is used in component qualification to reproduce operational responses in the laboratory. It is often preferred to single-input and base-shake testing because of the potential for equivalent or better tests using smaller actuators and shorter test suites. Given a target response, two key steps in MIMO test design are selecting actuator locations and solving for input loads. Actuator locations are often manually selected using expert judgment. If an automatic method is used, locations are usually determined by simulating the vibration control problem and minimizing a combination of the input energy and control residuals. To select a configuration, the relative importance of input energy and residuals must be specified. Specifying relative weights is, in general, a manual and subjective process. This paper develops an objective function that compares actuator configurations based on control accuracy and required input energy without any manual parameter tuning. The objective function uses an optimally selected tradeoff parameter for each candidate configuration. To choose actuator locations using the new objective function, a pivoting algorithm for integer programming problems is developed. Starting with an initial configuration (such as the one generated by a greedy algorithm), the pivoting algorithm guarantees an objective function decrease in each iteration until convergence is reached. In a simulation featuring a structure excited by a diffuse acoustic field, electrodynamic shaker locations and regularized inputs are solved for without any analyst-specified parameters. Simulations are performed in MIMO configurations where the number of target responses is less than, equal to, and greater than the number of actuators.

Keywords: Multi-input multi-output; shaker placement; Tikhonov regularization; greedy algorithm; integer programming

Received on December 18, 2024, Accepted on April 24, 2025, Published on May 5, 2025

1 Introduction

Multi-input, multi-output (MIMO) testing has grown in popularity for aerospace and automotive applications in the last two decades. By mimicking operational conditions in the laboratory, component and system qualification are significantly improved. MIMO testing is most often performed by suspending a test article from low-stiffness bungees or from cables [1, 2]. For some field loading configurations (especially aerodynamic and acoustic loading), well-designed MIMO tests yield far better replication of operational responses than single-axis or shaker-table testing [3].

MIMO testing is typically performed using multiple electrodynamic shakers [4, 5], but it can also be performed using piezoelectric actuators [6]. In either case, the location of actuators must be selected to yield a test that can safely produce the most representative target response possible. In the simplest case, engineering judgment can be used to place actuators on the structure, but a more repeatable and rigorous method is often desired. If a system model is available (such as a finite element model or an experimental model from modal testing), actuator locations

*keaton.coletti@uga.edu

†ben.davis@uga.edu

‡rschult@sandia.gov

can be chosen from among candidates using frequency response functions (FRFs) or system mode shapes. Some methods directly rely on modal analysis, including mode shape-based placement [7] and effective independence [8, 9]. Other methods perform control simulations using sets of candidate locations. Beale *et al.* considered the uncertainty of estimated inputs to assign weights to and subsequently downselect control locations [10], similar to how the Kullback-Leibler divergence metric is used for sensor placement [11]. Most often, the residuals between the simulated MIMO output and the target response are used as the objective. The residuals can be converted to a scalar by simple least squares or by an RMS decibel difference of the autospectra across frequencies and degrees of freedom [9, 12].

However, only considering control accuracy ignores the input energies. Often, as the number of actuators is increased, the required inputs to control to the target response also increase [9, 13]. Instead of working together, actuators can offset each other's modal contributions for some modes, leading to lower residuals but very large inputs. Mathematically, this corresponds to an increase in the condition number of the frequency response matrix (FRM). Because the loads that actuators can provide are limited, the required input energies are often infeasible or risk over-exciting unmeasured locations. Although inputs can be reduced by regularizing the control problem, there is no guarantee that the actuator locations provided by the residual objective will yield good control or small input energies when the regularization is applied. This motivates the inclusion of information about input energies during location selection. Kondoh *et al.* used a multivariate objective function to balance control and input force to place sensors and actuators [14]. Mayes *et al.* augmented this approach for shaker placement or control using electrodynamic models of shakers [13]. A major disadvantage of using multiple objectives is that the trade-off parameter must be specified prior to placing the actuators. Determining the weights on input magnitudes versus residuals is difficult, if not impractical, without knowing the MIMO configuration.

Regardless of the objective, placing actuators given a set of candidate locations is a difficult integer programming problem. Integer programming is a general descriptor for optimization problems with integer variables. In this case, the domain of the optimization variables is the discretized candidate locations. If the number of candidates and actuators are small, an exhaustive search can be performed. However, the number of unique configurations grows combinatorially, and this approach becomes computationally infeasible even for modest problems [7, 15]. Integer programming is a significant area of research in applied math and computer science, and probably the most commonly used algorithm for actuator placement is the greedy algorithm [16, 13]. In the greedy algorithm, input locations are selected one by one until a quota is filled. Each additional location is selected as the one minimizing an objective (usually residuals or a balance of residuals and inputs) among all candidates. Algorithms used for condition number minimization and effective independence can be considered a kind of "reverse greedy algorithm", wherein locations are progressively removed from a starting set until the quota is filled [10]. In other fields, greedy algorithms have been augmented with, *e.g.*, genetic algorithm crossovers [17], but these methods have not been used in MIMO testing.

After actuators are placed, they must be controlled to reproduce the output target response. Open and closed-loop control are both used, and closed-loop control is more common for random vibration testing [9]. Closed-loop control essentially involves solving the open-loop problem, applying the derived inputs, and adjusting inputs using the output residuals [18]. In any case, initial system inputs must be solved. The system FRMs may be ill-conditioned, and output target data are noisy, so a simple pseudoinverse often generates very large inputs. Regularization is typically used to deal with this ill-conditioning. [19, 20, 9, 21, 22].

Three common types of MIMO tests are time waveform replication, random vibration, and sine control. Random vibration involves control to a power spectral density (PSD) matrix [23, 24, 25]. Sine control [26] involves control to sinusoids with prescribed frequencies, amplitudes, and phases at multiple control channels. Time waveform replication (TWR) involves control to a time-domain waveform, typically solved in the frequency domain using the discrete Fourier transform [27]. The problem form addressed in this paper is the TWR problem. However, the random control problem can be converted to a TWR-like problem by synthesizing waveforms from the target PSD and controlling to the waveforms directly. Likewise, transient sinusoids can be converted to time-domain waveforms, so our methods can be applied to random and sine tests as well.

This paper is organized as follows. Section 2 provides relevant theory, including the problem definition, a new actuator-placement objective function that enables simultaneous comparison of input magnitude and residuals across input configurations, and an automatic method for selecting a Tikhonov regularization parameter for a given configuration. The automatically selected parameter can be passed into the new objective function to evaluate configurations without any parameter specification by the analyst. In Section 3, computational methods are discussed, and a new integer programming algorithm is described for solving the actuator placement problem. Section 4 verifies the new methods in a simulation wherein the output target is derived by applying a diffuse acoustic field to a shell with an internal tiered structure. Section 5 gives concluding remarks.

2 Theory

2.1 Problem setup

2.1.1 Problem definition and notation

The task addressed by this paper is to use N_i input channels to generate N_o known target responses. In some cases, multiple waveforms may be tested using a single shaker configuration, corresponding (for example) to different events in the life cycle of a structure. These “data frames” are represented by the index $j = 1, 2, \dots, N_r$, and the frequency-domain target responses are denoted $\mathbf{y}_j(\omega_k) \in \mathbb{C}^{N_o}$, $k = 1, 2, \dots, N_f$. The collection of all target data is denoted by $\mathbf{Y}(\omega_k) \in \mathbb{C}^{N_o \times N_r}$. Accurate frequency response functions (FRFs), $\mathbf{H}(\omega_k) \in \mathbb{C}^{N_o \times N_{\text{dof}}}$, are assumed known. N_{dof} is the number of candidate locations available for actuator placement. For brevity, we denote dependence on frequency using the subscript \circ_k , so the j^{th} data frame and k^{th} frequency index of response data is denoted $\mathbf{y}_j(\omega_k) \equiv \mathbf{y}_{jk}$. The symbol \mathbf{Y} is used as shorthand for the collection of all response data.

Selected shaker locations are contained in the set \mathcal{L} , and the respective columns in \mathbf{H}_k are retained to produce $N_o \times N_i$ frequency response matrices, denoted by $\mathbf{H}_k(\mathcal{L})$. The frequency-domain shaker inputs, denoted \mathbf{X} , must also be derived. Typically, two objectives are considered: the magnitude of squared residuals and the input energy. Formally, the dual-objective optimization problem is described as

$$\begin{aligned} \min_{\mathcal{L}, \mathbf{X}_k} \quad & \left\langle \sum_k \|\mathbf{Y}_k - \mathbf{H}_k(\mathcal{L}) \mathbf{X}_k\|_F^2, \sum_k \|\mathbf{X}_k\|_F^2 \right\rangle \\ \text{s.t.} \quad & \text{card}(\mathcal{L}) = N_i \end{aligned} \quad (1)$$

Here $\text{card}(\circ)$ denotes the cardinality (the number of elements in a set), and $\|\circ\|_F$ is the Frobenius norm. As is standard for multi-objective optimization problems, a Pareto frontier can be produced by defining a tradeoff parameter and solving

$$\begin{aligned} \min_{\mathcal{L}, \mathbf{X}_k} \quad & \sum_k \|\mathbf{Y}_k - \mathbf{H}_k(\mathcal{L}) \mathbf{X}_k\|_F^2 + \lambda \sum_k \|\mathbf{X}_k\|_F^2 \\ \text{s.t.} \quad & \text{card}(\mathcal{L}) = N_i. \end{aligned} \quad (2)$$

Each solution to Eq. (2) is Pareto-optimal, and every Pareto-optimal solution to Eq. (1) is a solution to Eq. (2) for some λ . Hence, the combined objective function captures every potentially desirable solution to the multi-objective optimization problem. Although independent tradeoff parameters can be set at each frequency, unequal values generally yield a non-Pareto-optimal solution. That is, if the tradeoff parameters are unequal, there will always be another solution that yield lower inputs, lower residuals, or both. Defining λ_k as a function of frequency has the effect of weighting some source components more than others. The resulting minimum is, in general, not a minimum value for some fixed λ and is thus strictly dominated.

2.1.2 Discussion

For a fixed \mathcal{L} , λ is the Tikhonov regularization parameter, and a closed-form solution is available for \mathbf{X} . Methods for selecting λ include the L-curve [28], the generalized cross-validation, and empirical Bayesian approaches [19]. These approaches rely on a fixed $\mathbf{H}_k(\mathcal{L})$, but \mathcal{L} is unknown during the experiment design. Hence, the input locations must be selected prior to source estimation. But the choice of \mathcal{L} depends on λ , leading to an apparent paradox: \mathcal{L} must be known to solve for λ , but λ must be known to solve for \mathcal{L} .

Two approaches can be taken to address this problem. The first is to simply set $\lambda = 0$ and solve for \mathcal{L} . Then, the L-curve or other approaches can be used to update λ and \mathbf{X} . The resulting configuration ignores the source magnitude, so it can be sub-optimal when the regularization parameter is updated. Another method is to define a set of values for λ and optimize input locations for each value. The resulting candidate sets can be used to build a Pareto frontier. This approach can yield significant improvements over the least-squares approach, but the resulting Pareto frontier is comprised of solutions from multiple $\mathbf{H}_k(\mathcal{L})$, so automatic parameter selection approaches fail. The only option is to build the Pareto frontier and to manually select a location.

A reasonable improvement would be to automatically select λ for every candidate \mathcal{L} during the optimization procedure. In an appropriate optimization algorithm, such an approach would enable selection of \mathcal{L} and \mathbf{X} without needing to specify λ prior to optimization. However, Eq. (2) is not applicable across different values of λ . Take as an example two solutions for \mathcal{L} that yield identical input and residual norms but use different regularization parameters.

The configuration with the lower value of λ will be rated as superior even though the solutions are equivalent. Using this objective, configurations that prefer smaller values of λ are always preferred, even if they yield larger input magnitudes. Section 2.3 derives an alternative objective function that can be used to compare location sets without any prior specification of λ .

2.2 Probability toolkit

Here, we provide a brief overview of probabilistic notation and identities used in the remainder of Section 2. For a more comprehensive review and introduction, see Ref. [29]. First, assume we have random variables A and B . We denote the conditional probability density function of A given B (with some shorthand) by

$$p(a|b) \equiv p(A = a|B = b). \quad (3)$$

This notation is fairly standard in engineering [29]. Denote in particular the circular complex Gaussian distribution [30] by

$$\mathcal{N}(\mathbf{x}|\boldsymbol{\mu}, \boldsymbol{\Omega}) \propto |\boldsymbol{\Omega}|^{-1} e^{-(\mathbf{x}-\boldsymbol{\mu})^H \boldsymbol{\Omega}^{-1}(\mathbf{x}-\boldsymbol{\mu})}. \quad (4)$$

Here \propto denotes proportionality when constants can be ignored in probability density expressions, and \circ^H is the conjugate transpose. $\boldsymbol{\Omega}$ and $\boldsymbol{\mu}$ are the mean and covariance of the normal distribution, respectively. A basic operation is multiplication of marginal distributions to form a joint distribution:

$$p(a, b|c) = p(a|b, c) p(b|c). \quad (5)$$

We will also use Bayes' rule, given by

$$p(b|a) = \frac{p(a|b) p(b)}{p(a)} \propto p(a|b) p(b). \quad (6)$$

The left side is called the "posterior", $p(a|b)$ is the "likelihood", $p(b)$ is the "prior", and $p(a)$ is the "evidence". The evidence is typically neglected in favor of the proportional form on the right side of Eq. (6). Finally, an important identity is marginalization, whereby a random variable is removed from a joint distribution,

$$p(a|c) = \int_{\mathcal{B}} p(a, b|c) db, \quad (7)$$

where \mathcal{B} is the domain of b .

2.3 Regularization-agnostic objective function

In this subsection, we derive an objective function that can be used to directly compare configurations \mathcal{L} for any given value of the tradeoff parameter, λ . For a fixed tradeoff parameter, the objective is the same as in Eq. (2). First, define the (prior) probability of the inputs \mathbf{X} as

$$p(\mathbf{X}|\sigma_x) = \prod_{j,k} \mathcal{N}(\mathbf{x}_{j,k} | \mathbf{0}, \sigma_x \boldsymbol{\Sigma}_x). \quad (8)$$

Because this Gaussian distribution is zero-mean, smaller inputs are preferred. Because the covariance is $\sigma_x \boldsymbol{\Sigma}_x$, smaller values of σ_x indicate a stricter penalty on the size of \mathbf{X} . $\boldsymbol{\Sigma}_x$ is a user-defined matrix that determines the relative penalties on the size of the inputs and correlations between the inputs. Next, define the likelihood of the target response given a shaker configuration and inputs by

$$p(\mathbf{Y}|\mathcal{L}, \mathbf{X}, \sigma_n) = \prod_{j,k} \mathcal{N}(\mathbf{y}_{j,k} | \mathbf{H}_k(\mathcal{L}) \mathbf{x}_{j,k}, \sigma_n \boldsymbol{\Sigma}_n). \quad (9)$$

Here, σ_n scales the noise term (or more generally, the error between modeled and actual response). $\boldsymbol{\Sigma}_n$ is a user-defined matrix that determines the covariance structure of the noise. If $\boldsymbol{\Sigma}_x$ and $\boldsymbol{\Sigma}_n$ are defined as functions of frequency, they can be replaced by $\boldsymbol{\Sigma}_n(\omega_k)$ and $\boldsymbol{\Sigma}_x(\omega_k)$. In most applications, $\boldsymbol{\Sigma}_n = \boldsymbol{\Sigma}_x = \mathbf{I}$ uniformly. Now, set $p(\mathcal{L}) \propto 1$. Applying Bayes' Theorem yields

$$\begin{aligned} p(\mathcal{L}, \mathbf{X}|\mathbf{Y}, \sigma_n, \sigma_x) &\propto p(\mathcal{L}, \mathbf{Y}|\mathbf{X}, \sigma_n) p(\mathbf{X}|\sigma_x) \\ &\propto p(\mathbf{Y}|\mathcal{L}, \mathbf{X}, \sigma_n) p(\mathbf{X}|\sigma_x). \end{aligned} \quad (10)$$

Eq. (10) gives the joint probability of the input loads and actuator locations. Next, define the variable $\lambda = \sigma_n/\sigma_x$, which represents the ratio of noise energy to input energy [19]. We will later show that this parameter is the same as λ in Section 2.1. Performing the change of variables $\sigma_n = \sigma_x\lambda$ and multiplying by $p(\sigma_x) \propto 1$ gives

$$p(\mathcal{L}, \mathbf{X}, \sigma_x | \mathbf{Y}, \lambda) \propto p(\mathcal{L}, \mathbf{X} | \mathbf{Y}, \sigma_n, \sigma_x) |_{\sigma_n = \sigma_x \lambda}. \quad (11)$$

Substituting Eqs. (8) and (9) into Eq. (11), taking the negative natural logarithm, and removing constants yields

$$\begin{aligned} -\ln p(\mathcal{L}, \mathbf{X}, \sigma_x | \mathbf{Y}, \lambda) = & N_i N_r N_f \ln(\sigma_x) + N_o N_r N_f \ln(\sigma_x \lambda) + \frac{1}{\sigma_x} \sum_{j,k} \mathbf{x}_{jk}^H \boldsymbol{\Sigma}_x^{-1} \mathbf{x}_{jk} \\ & + \frac{1}{\sigma_x \lambda} \sum_{j,k} (\mathbf{y}_{jk} - \mathbf{H}_k(\mathcal{L}) \mathbf{x}_{jk})^H \boldsymbol{\Sigma}_n^{-1} (\mathbf{y}_{jk} - \mathbf{H}_k(\mathcal{L}) \mathbf{x}_{jk}). \end{aligned} \quad (12)$$

Eq. (12) can be minimized to give the best shaker locations and inputs, as well as the most likely source level σ_x . The minimizing values of \mathbf{X} and σ_x have closed-form solutions. If we fix \mathcal{L} and σ_x , the minimum of Eq. (12) over \mathbf{X} is a well-known solution:

$$\hat{\mathbf{X}}_k(\mathcal{L}; \lambda) = \mathbf{H}^+(\mathcal{L}; \lambda) \mathbf{Y}_k, \quad (13)$$

where $\mathbf{H}^+(\mathcal{L}; \lambda)$ is the “regularized pseudoinverse” of $\mathbf{H}(\mathcal{L})$, the standard solution to the Tikhonov regularization problem in Eq. (2). See Table 1 for more details. Using this definition, define the inversely-estimated source metric (\hat{s}) and residual metric (\hat{r}) as

$$\hat{s}(\mathcal{L}; \lambda) = \sum_{j,k} \hat{\mathbf{x}}_{jk}^H \boldsymbol{\Sigma}_x^{-1} \hat{\mathbf{x}}_{jk}, \quad (14)$$

$$\hat{r}(\mathcal{L}; \lambda) = \sum_{j,k} (\mathbf{y}_{jk} - \mathbf{H}_k(\mathcal{L}) \hat{\mathbf{x}}_{jk})^H \boldsymbol{\Sigma}_n^{-1} (\mathbf{y}_{jk} - \mathbf{H}_k(\mathcal{L}) \hat{\mathbf{x}}_{jk}). \quad (15)$$

Function arguments \mathcal{L} and λ are hereafter neglected for brevity. Defining $a = N_o N_r N_f$ and $b = N_i N_r N_f$, Eq. (12) can be concisely rewritten as

$$-\ln p(\mathcal{L}, \hat{\mathbf{X}}, \sigma_x | \mathbf{Y}, \lambda) = a \ln(\sigma_x \lambda) + b \ln(\sigma_x) + \frac{\hat{r}}{\sigma_x \lambda} + \frac{\hat{s}}{\sigma_x}. \quad (16)$$

Now, minimizing over σ_x by setting the derivative with equal to zero and solving yields

$$\hat{\sigma}_x = \frac{\hat{r}/\lambda + \hat{s}}{a + b}. \quad (17)$$

Substituting into Eq. (16) and simplifying yields the remarkably simple objective function,

$$f(\mathcal{L}; \lambda) = \ln(\hat{r} + \lambda \hat{s}) - \frac{b}{a + b} \ln \lambda, \quad (18)$$

which represents

$$f(\mathcal{L}; \lambda) = \arg \min_{\mathbf{X}, \sigma_x} -\ln p(\mathcal{L}, \mathbf{X}, \sigma_x | \mathbf{Y}, \lambda). \quad (19)$$

For a fixed value of λ and with $\boldsymbol{\Sigma}_n = \boldsymbol{\Sigma}_x = \mathbf{I}$, Eq. (18) reduces to the simple Tikhonov objective in Eq. (2). However, it includes an additional term that penalizes smaller values of λ , removing the erroneous effect discussed in Section 2.1.2.

2.4 Selecting the regularization parameter

A simple strategy for selecting λ is to maximize the joint distribution, $p(\mathcal{L}, \hat{\mathbf{X}}, \hat{\sigma}_x, \lambda | \mathbf{Y}) \propto p(\mathcal{L}, \hat{\mathbf{X}}, \hat{\sigma}_x | \mathbf{Y}, \lambda)$, with respect to λ . The objective in words is then to pick the \mathcal{L} , σ_n , σ_x , and \mathbf{X} that maximize the joint density of \mathbf{X} and \mathbf{Y} . However, $f \rightarrow -\infty$ as $\lambda \rightarrow \infty$ because as $\sigma_x \rightarrow 0$, the density of $\mathbf{X} = \mathbf{0}$ is infinite, but \hat{r} is bounded. The optimal solution is

Quantity	Expression
$\hat{\mathcal{L}}$	$\arg \min_{\mathcal{L}} \ln (\hat{r} + \hat{\lambda} \hat{s}) - \frac{b}{a+b} \ln \hat{\lambda}$
$\hat{\mathbf{X}}_k$	$\Sigma_x^{1/2} \mathbf{V}_k (\mathbf{S}_k^2 + \hat{\lambda} \mathbf{I})^{-1} \mathbf{S}_k \mathbf{U}_k^H \Sigma_n^{-1/2} \mathbf{Y}_k$
$\hat{\lambda}$	$\arg \min_{\lambda} N_r \sum_{k,l} \ln (d_{kl} + \lambda) + (a - 2) \ln \sum_{k,l} \frac{z_{kl}}{d_{kl} + \lambda}$
\hat{r}	$\sum_{j,k} (\mathbf{y}_{jk} - \mathbf{H}_k \hat{\mathbf{x}}_{jk})^H \Sigma_n^{-1} (\mathbf{y}_{jk} - \mathbf{H}_k \hat{\mathbf{x}}_{jk})$
\hat{s}	$\sum_{j,k} \hat{\mathbf{x}}_{jk}^H \Sigma_x^{-1} \hat{\mathbf{x}}_{jk}$
a, b	$a = N_o N_r N_f, b = N_i N_r N_f$
d_{kl}	$\left[\bar{\mathbf{S}}_k \bar{\mathbf{S}}_k^H \right]_{ll}, l = 1, 2, \dots, N_o$
z_{kl}	$\sum_j [\bar{\mathbf{u}}_k]_l^H \Sigma_n^{-1/2} \mathbf{y}_{jk}$
$\mathbf{U}_k, \mathbf{S}_k, \mathbf{V}_k$	$\Sigma_n^{-1/2} \mathbf{H}_k \Sigma_x^{1/2} = \mathbf{U}_k \mathbf{S}_k \mathbf{V}_k^H = \bar{\mathbf{U}}_k \bar{\mathbf{S}}_k \bar{\mathbf{V}}_k^H$

Table 1: Relevant quantities and objective functions for determining input locations, $\hat{\mathcal{L}}$, and loads, $\hat{\mathbf{X}}$. Here \circ and $\bar{\circ}$ denote the compact and standard singular value decompositions, and $[\bar{\mathbf{u}}_k]_l$ is row l of $\bar{\mathbf{u}}$.

then to set $\lambda = \infty$ and $\mathbf{X} = \mathbf{0}$, in which case all \mathcal{L} are equivalent. Clearly, then, λ must be specified independently of Eq. (18).

Any existing method could be used to select λ , e.g., the L-curve or generalized cross validation. In this paper, a Bayesian method is used. The derivation is based on Ref. [19], but it is modified to identify a single regularization parameter over multiple frequencies. The explicit details are omitted from this section but are shown in Appendix A. The principle is to select

$$\hat{\lambda} = \arg \min_{\lambda} -\ln p(\lambda | \mathbf{Y}). \quad (20)$$

This is equivalent to minimizing

$$g(\lambda) = N_r \sum_{k,l} \ln (d_{kl} + \lambda) + (a - 2) \ln \sum_{k,l} \frac{z_{kl}}{d_{kl} + \lambda}. \quad (21)$$

The quantities z_{kl} and d_{kl} , $l = 1, 2, \dots, N_o$, are given in Table 1. In the special case wherein $N_f = 1$, Eq. (21) is the same objective function as the one given by Ref. [19]. An algorithm for efficient minimization of Eq. (21) is given in Appendix B. Using Eq. (18), $\hat{\mathcal{L}}$ and $\hat{\mathbf{X}}$ are found by minimizing $f(\mathcal{L}; \hat{\lambda}(\mathcal{L}))$ over \mathcal{L} . Table 1 summarizes all relevant quantities in computationally efficient forms and is intended to aid implementation.

3 Computation

Minimization over \mathcal{L} is a nonlinear integer programming problem. In MIMO testing, Eq. (2) is often minimized using a greedy algorithm. Starting with the empty set, the greedy algorithm evaluates $\mathcal{L} \cup c$ for each candidate input location c . The best location is appended to \mathcal{L} , and the procedure continues until N_i locations are selected.

3.1 Improvements to the greedy algorithm using optimal pivoting

An initial estimate of \mathcal{L} can be significantly improved by replacing entries iteratively to improve the objective function. Let $\mathcal{L}_t \setminus \{n\}$ be the n^{th} item in the set in iteration t . A reasonable value of \mathcal{L}_0 is the output from a standard greedy algorithm. Define $\mathcal{L}_t^{-n} = \mathcal{L}_t \setminus \{n\}$ to be the location set with the n^{th} entry removed. We define the ‘‘removal affinity’’ as

$$a_t(n, \emptyset) = f(\mathcal{L}_t^{-n}) - f(\mathcal{L}_t). \quad (22)$$

The removal affinity is the change in objective if $\mathcal{L} \setminus \{n\}$ is removed from \mathcal{L} . It is generally positive, meaning the objective is worse if a location is removed from the set. Also, let $c \in \{1, 2, \dots, N_{\text{dof}}\}$ and define the ‘‘replacement affinity’’ as

$$a_t(n, c) = f(\mathcal{L}_t^{-n} \cup c) - f(\mathcal{L}_t). \quad (23)$$

The replacement affinity is the change in objective function if $\mathcal{L}\{n\}$ is replaced with c .

The pivoting algorithm is described as follows. For each n in iteration t , $\hat{c}(n)$ is defined as the c with the minimum replacement affinity (since we are minimizing), $\min_c \{a_t(n, c)\}$. This is the best replacement for the n^{th} entry in \mathcal{L}_t , which may be $\mathcal{L}_t\{n\}$ itself. Then, $a_t(n, \emptyset)$ is calculated for each n . The n with minimum removal affinity such that $a_t(n, \hat{c}(n)) < -\varepsilon$ is selected to be replaced and is named \hat{n} . By construction, this forbids $\hat{c}(\hat{n}) = \mathcal{L}\{\hat{n}\}$ and guarantees improvement by ε in each iteration. The location set is updated by $\mathcal{L}_{t+1} = \mathcal{L}_t^{-\hat{n}} \cup \hat{c}(\hat{n})$. Iterations stop when \hat{n} cannot be selected, i.e., $a_t(c, n) \geq -\varepsilon$ for all c and n , or when an iteration limit is reached.

Each step in the pivoting algorithm amounts to picking the “least-important” shaker location in \mathcal{L} , removing it, and adding the best available alternative. If the best alternative is the location that was just removed, the second least important is removed instead, and so on.

In general, ε is specified near machine precision, and in most cases $\varepsilon = 0$ is appropriate. The constraint provided by ε prevents replacing an input location with itself because $a_t(\hat{n}, \mathcal{L}\{\hat{n}\}) = 0$: allowing such a replacement would lead to infinite iteration. It also prevents infinite iteration when multiple configurations yield identical objective function values or values that differ only by numerical error. Convergence in finite time is guaranteed (the discrete combinations of locations are finite, and repetition is prohibited), but a backup iteration limit prevents excessive computational cost. The pivoting algorithm is summarized in Algorithm 1.

Algorithm 1 Pivoting algorithm for integer programming with objective f and cardinality N_o

Initialize \mathcal{L}_0 using greedy algorithm or random selection

for $t = 0, 1, \dots, t_{\max} - 1$ **do**

for $n = 1, 2, \dots, N_o$ **do**

 Calculate $a_t(n, c)$ for each candidate c

 Select $\hat{c}(n) = \arg \min_c \{a_t(n, c)\}$ and retain $a_t(n, \hat{c}(n))$

 Calculate $a_t(n, \emptyset)$ and retain

end for

 Assign $\hat{n} = \arg \min_n \{a_t(n, \emptyset) \mid a_t(n, \hat{c}(n)) < -\varepsilon\}$

if \hat{n} is empty **then**

 Terminate for-loop

else

 Assign $\mathcal{L}_{t+1} = \mathcal{L}_t^{-\hat{n}} \cup \hat{c}(\hat{n})$

end if

end for

3.2 Fast computation of the least-squares objective

Although this paper does not restrict f to a least squares objective (Eq. (2) with $\lambda = 0$), it is a common method for placing actuators. In this special case, computation of $f(\mathcal{L} \cup c)$ can be greatly accelerated if multiple c are to be evaluated. This acceleration is applicable to the pivoting algorithm and to the greedy algorithm, which progressively builds \mathcal{L} by starting with the empty set and then evaluating $f(\mathcal{L} \cup c)$ for each c not already in \mathcal{L} . For the least-squares case, the only component of f to calculate is \hat{r} , the sum of (weighted) squared residuals. In each frequency bin, because $\hat{\mathbf{X}}_k$ is given by the non-regularized pseudoinverse, we can write the residuals as

$$\mathbf{R}_k(\mathcal{L}) = \mathbf{Y}_k - \mathbf{H}_k(\mathcal{L})\hat{\mathbf{X}}_k = \mathbf{Y}_k - \text{proj}_{\mathbf{H}_k(\mathcal{L})} \mathbf{Y}_k \quad (24)$$

Here, $\text{proj}_A \mathbf{B}$ denotes the projection of the columns of \mathbf{B} onto the column space of \mathbf{A} . The projection is given by $\text{proj}_A \mathbf{B} = \text{col}(\mathbf{A}) \text{col}(\mathbf{A})^H \mathbf{B}$, where $\text{col}(\circ)$ outputs an orthonormal basis for the column space. Acceleration is achieved by applying the identity

$$\mathbf{R}_k(\mathcal{L} \cup c) = \mathbf{R}_k(\mathcal{L}) - \text{proj}_{\mathbf{N}_k(c)} \mathbf{R}_k(\mathcal{L}), \quad (25)$$

using the definition

$$\mathbf{N}_k(c) = \text{proj}_{\text{null}(\mathbf{H}_k(\mathcal{L}))} \mathbf{H}_k(c), \quad (26)$$

which is proven in Appendix C. This calculation is very fast, even when N_{dof} is large. For a fixed \mathcal{L} , the residuals and nullspace of $\mathbf{H}_k(\mathcal{L})$ need only be calculated once. Recall also that $\mathbf{H}_k(c)$ is the c^{th} column of \mathbf{H}_k , so $\mathbf{N}_k(c)$ is a

column vector whose orthonormal basis is itself multiplied by a constant. Calculating the residuals for frequency bin k across all c (which could be thousands) then amounts to one residual calculation, one nullspace calculation, one matrix multiplication, N_{dof} vector subtractions, and two times N_{dof} vector multiplications. Without this procedure, N_{dof} pseudoinverse calculations would be required. The computation steps are summarized in Algorithm 2 for the case when $\Sigma_n = \mathbf{I}$. Other cases are not addressed in this paper, but a similar computational approach could be combined with a noise-whitening step.

Algorithm 2 Calculating the updated least-squares objective, $f(\mathcal{L} \cup c; \lambda = 0)$, for $c = 1, 2, \dots, N_{\text{dof}}$.

```

for  $k = 1, 2, \dots, N_f$  do                                ▶ Loops can be parallelized or computed with multi-axis arrays
    Calculate  $\mathbf{R}_k = \mathbf{Y}_k - \text{proj}_{\mathbf{H}_k(\mathcal{L})} \mathbf{Y}_k$ 
    Calculate  $\mathbf{N}_k = \text{proj}_{\text{null}(\mathbf{H}_k(\mathcal{L}))} \mathbf{H}_k$                                 ▶  $\mathbf{H}_k \in \mathbb{C}^{N_o \times N_{\text{dof}}}$  is the global FRM
    Normalize  $\mathbf{N}_k$  so that  $\text{diag}(\mathbf{N}_k^H \mathbf{N}_k)$  contains ones                                ▶ Set column norms to 1 for projection operation
    for  $c = 1, 2, \dots, N_{\text{dof}}$  do
        Calculate  $\mathbf{R}_k(c) = \mathbf{R}_k - \mathbf{N}_k(c) \mathbf{N}_k^H(c) \mathbf{R}_k$                                 ▶  $\mathbf{N}_k(c)$  is column  $c$  of  $\mathbf{N}_k$ 
    end for
end for

for  $c = 1, 2, \dots, N_{\text{dof}}$  do
    Output  $f(\mathcal{L} \cup c; \lambda = 0) = \sum_k \|\mathbf{R}_k(c)\|_F$ 
end for

```

3.3 Solution methods

The remainder of this section describes high-level procedures used to estimate input locations and loads. The simplest solution approach is to evaluate $f(\mathcal{L}; \hat{\lambda}(\mathcal{L}))$ directly and optimize over \mathcal{L} . The input to the pivoting algorithm (\mathcal{L}_0) is derived using the greedy algorithm. When $\hat{\mathcal{L}}$ is determined, $\hat{\mathbf{X}}$ is immediately available. This approach is hereafter named “automatic Tikhonov” or “auto”.

If the FRM is well-conditioned, the inverse solution is less sensitive to regularization, and the unregularized solution ($\lambda = 0$) may be reasonably close to the regularized solution ($\lambda = \hat{\lambda}$). In such cases, the combined greedy and pivoting algorithms can be applied to $f(\mathcal{L}; \lambda = 0)$ at great computational advantage. After $\hat{\mathcal{L}}$ is determined, $\hat{\lambda}(\hat{\mathcal{L}})$ and $\hat{\mathbf{X}}(\hat{\mathcal{L}})$ are calculated from Table 1. In other words, the shaker locations are determined assuming that no regularization will be used, and then the parameter is updated using the selected locations. This approach is hereafter named “least squares” or “LSTSQ”.

Although the pivoting algorithm offers improvement over an initial estimate, it does not guarantee optimality because local minima are possible. It may be beneficial in some cases to increase diversity by drawing several candidate local optima and choosing the best one. Along these lines, a set of regularization parameters can be pre-defined by the analyst, and the greedy-pivoting combination algorithm can be applied to $f(\mathcal{L}; \lambda_{\text{fixed}})$. This results in as many configuration candidates as pre-defined λ . Then, $f(\mathcal{L}; \hat{\lambda}(\mathcal{L}))$ can be evaluated for each configuration. The values of λ are defined in this paper on a logarithmic grid between $10^{-5} \times \hat{\lambda}_{\text{LSTSQ}}$ and $10^5 \times \hat{\lambda}_{\text{LSTSQ}}$. This method is hereafter named “fixed Tikhonov” or “fixed”.

4 Simulation demonstration

4.1 Simulation setup

The simulation structure is a cylindrical shell with diameter 50 cm, length 65.75 cm, and thickness 0.75 cm. Fixed to its base is an internal tiered structure. The assembly is pictured in Fig. 1. The material properties of the entire assembly are similar to steel, with a Young’s modulus of 200 GPa, Poisson’s ratio of 0.29, and density of 7800 kg/m³. The cylinder is fixed along both rims but is free on the lower surface for radii less than the outer radius minus 0.75 cm. The first 100 modes are solved, and 1% modal damping is assigned. The natural frequency of the 100th mode is 1892 Hz. The response targets, \mathbf{y}_{jk} , are randomly synthesized using the cross-power spectral density $\mathbf{S}_{yy}(\omega_k) = \mathbf{H}_k \mathbf{S}_{xx}(\omega_k) \mathbf{H}_k^H$, where \mathbf{H}_k has N_o rows and as many columns as finite element (FE) nodes on the exterior surface of the cylinder. Off-diagonal terms are not neglected, so the target response includes correlations between control channels. $\mathbf{S}_{xx}(\omega_k)$ is defined using the cylindrical scattering function for diffuse acoustic fields [31]. This simulation setup is created to

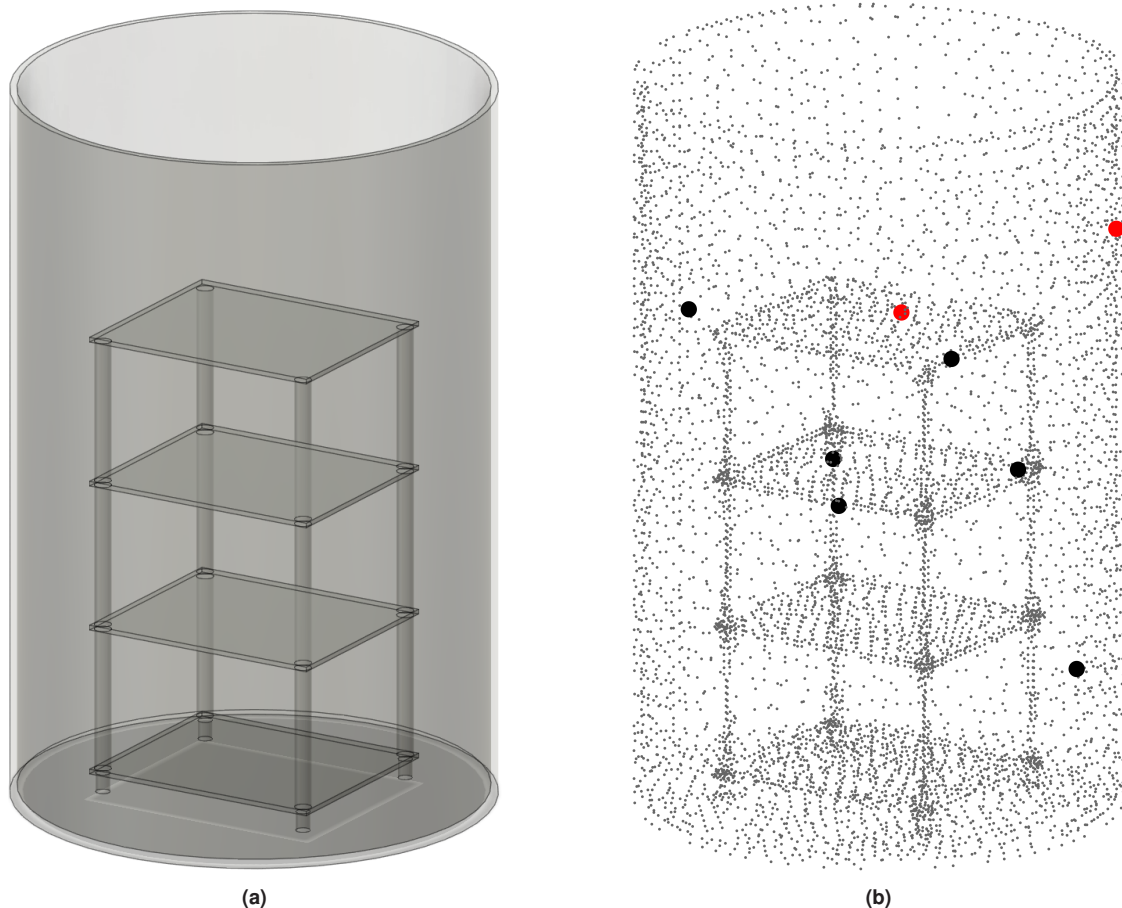


Fig. 1: Simulation structure and FE nodes. Red markers indicate triaxial accelerometer locations for the two-accelerometer cases in Fig. 3 and Fig. 4, and both red and black markers show locations in the eight-accelerometer cases. The cylindrical shell contains three black dots and one red dot.

demonstrate academic principles, but it is inspired by real structures, such as a rocket fairing with an internal circuit board tower.

Integer frequencies between 10 Hz and 1600 Hz are considered. To apply the diffuse acoustic field to the unevenly spaced FE mesh, the mode shapes are interpolated to the center points of a 30-longitudinal-division by 80-circumferential-division rectangular grid, and surface-normal components are calculated. Modal loads are calculated by premultiplying the surface-normal interpolated mode-shape matrix by diffuse field pressures at each center point times the area of each patch. Noise is added at a 30 dB signal-to-noise ratio, so the variance of the added noise for each entry in \mathbf{Y}_k equals $10^{-3} \frac{1}{N_o N_f} \sum_k \text{tr}(\mathbf{S}_{yy}(\omega_k))$. In Fig. 2, an example sum of target magnitudes for 24 accelerometer channels is plotted versus frequency. The plot appears jagged mostly because system inputs are randomly sampled from the diffuse field in each frequency bin, not because of added noise.

Candidate shaker inputs are restricted to the outer surface of the cylinder in the normal direction only. A total of 9,383 nodes are available as input locations. Only a subset of these nodes are considered for actuator placement, so random samples are drawn without replacement. Cases shown in this section use one realization ($N_r = 1$). Measurements are simulated at $N_o/3$ randomly placed triaxial accelerometers or N_o uniaxial accelerometers which can be located on the cylindrical shell or on the internal tiered structure.

4.2 Pareto optimality curves

To compare shaker configurations without directly inspecting the derived inputs, Pareto optimality curves are constructed. Constructing each curve involves first solving for shaker locations using the “LSTSQ”, “fixed”, and “auto” methods. The plot markers in Fig. 3 show the input energy and residuals for each method, using the greedy algorithm and greedy plus pivoting. Then, using the same shaker configurations, the residuals and input energy are plotted

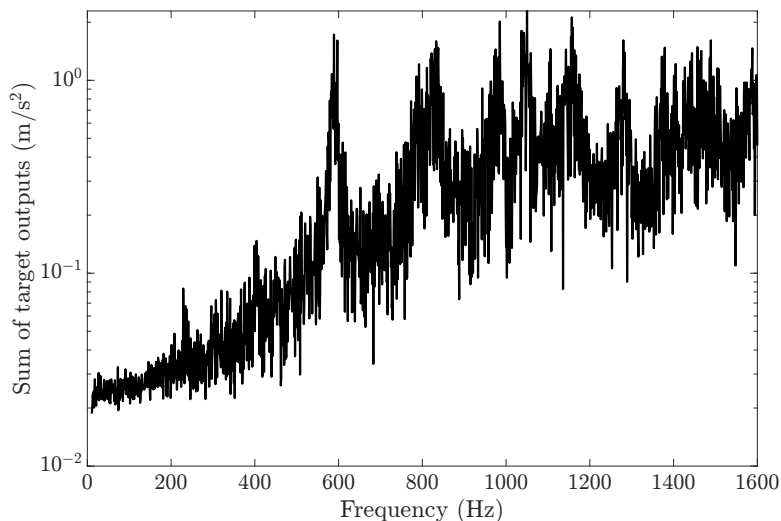


Fig. 2: Example sum of target accelerations for the simulation case with eight triaxial accelerometers.

for various values of λ . Fig. 3 shows several values of N_o and N_i with $N_{\text{dof}} = 500$. Fig. 4 shows the corresponding frequency-domain residuals and input energies for “LSTSQ greedy” and the subjective “best” cases, chosen manually by position relative to the other Pareto optimality curves. In the left column of Fig. 4, the squared residuals are normalized by the target PSD, resulting in a dimensionless error measure. For the “fixed” method, an intermediate output is a set of plausible configurations corresponding to λ_{fixed} . The corresponding optimality curves are shown in Fig. 5, and the curve minimizing $f(\hat{\mathcal{L}}|\lambda(\hat{\mathcal{L}}))$ is marked in black.

In the even-determined and under-determined cases (Fig. 3a and Fig. 3c), the target response is theoretically exactly achievable with any shaker configuration if a very large input is allowed. The least-squares objective, then, is quite meaningless. As a result, the “LSTSQ greedy” and “LSTQ pivot” algorithms give the same input configurations. For the “auto” and “fixed” methods, pivoting yields improvement, and control accuracy and input energies are improved after regularized inputs are solved. Fig. 3b in particular showcases the sub-optimality of the least-squares objective. The “LSTSQ” residuals are the lowest among all methods, but the input energy is much higher. “LSTSQ” only seeks to move the upper-left tail of the Pareto curve to the left, no matter the effect when regularized controls are solved.

4.3 Performance study

This section compares the performance of the previously described methods for simultaneous shaker placement and input estimation. Fig. 6 shows squared residuals and input energy for placement of five and eight shakers for several uniaxial accelerometer counts. All values are divided by $\hat{r}(\hat{\mathcal{L}})$ and $\hat{s}(\hat{\mathcal{L}})$ for the “LSTSQ greedy” algorithm, a method commonly used in practice. The means of the resulting ratios across ten trials are plotted.

The “LSTSQ pivot” method reduces residuals but does not improve results in general because it ignores input energy. This phenomenon is discussed in Section 4.2. The “auto” and “fixed” greedy methods are omitted from Fig. 6, but their results are consistently worse than the pivot methods. The “auto pivot” and “fixed pivot” algorithms consistently improve control accuracy and reduce total input energy across all frequency bins. With some exceptions, input energy is decreased the most when $N_o \geq N_i$, and residuals are decreased the most when $N_o < N_i$. For all tested configurations, optimizing $f(\mathcal{L}|\lambda)$ is significantly better than setting $\lambda = 0$ for experiment design.

In this simulation study, the FRFs were assumed to be known without error. In practice, there is always some error associated with structural FRFs. The effect of model uncertainty on the performance of the different methods is unknown, and future work should investigate this.

4.4 Computational cost

Fig. 7 shows the computational cost of the six solution methods for a range of N_{dof} . This case corresponds to the placement of six shakers using eight triaxial accelerometers, and an Intel 12900K processor and a MATLAB implementation were used. For this example, pivoting costs about six times as much as the greedy algorithm. The “fixed” method is significantly faster than the “auto” method when ten values of λ_{fixed} are used. This is because

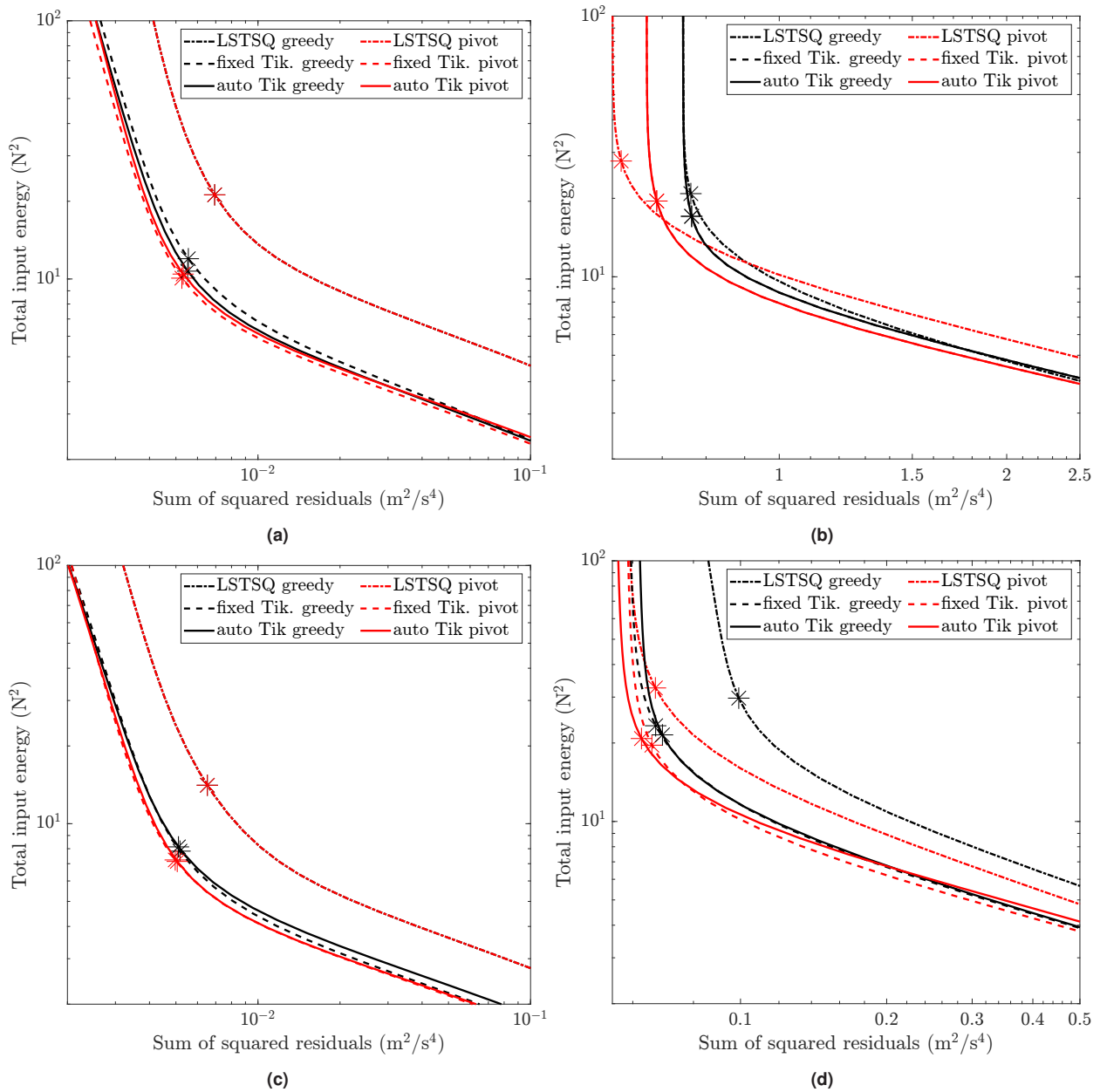


Fig. 3: Pareto optimality curves and optimal inputs (marked). $N_o/3$ triaxial accelerometers are used to place N_i shakers, and subfigures show problems that are (a) even-determined: $N_i = 6, N_o = 6$ (b) over-determined: $N_i = 3, N_o = 24$ (c) under-determined: $N_i = 8, N_o = 6$ (d) over-determined: $N_i = 8, N_o = 24$.

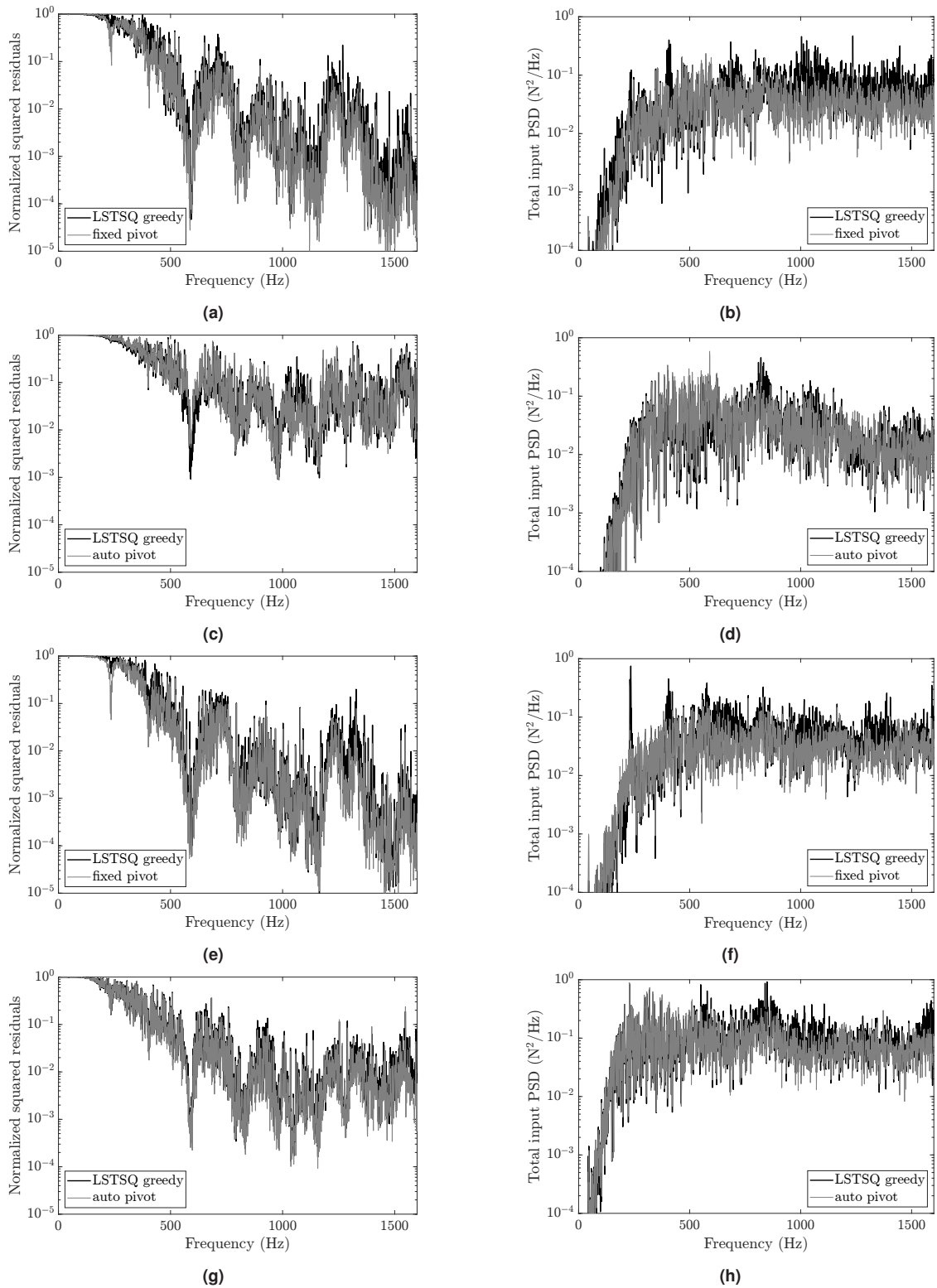


Fig. 4: Example of (left) squared control residuals and (right) input energies versus frequency for the cases in Fig. 3. Row 1 corresponds to (a) in Fig. 3, row 2 to (b), 3 to (c), and 4 to (d).

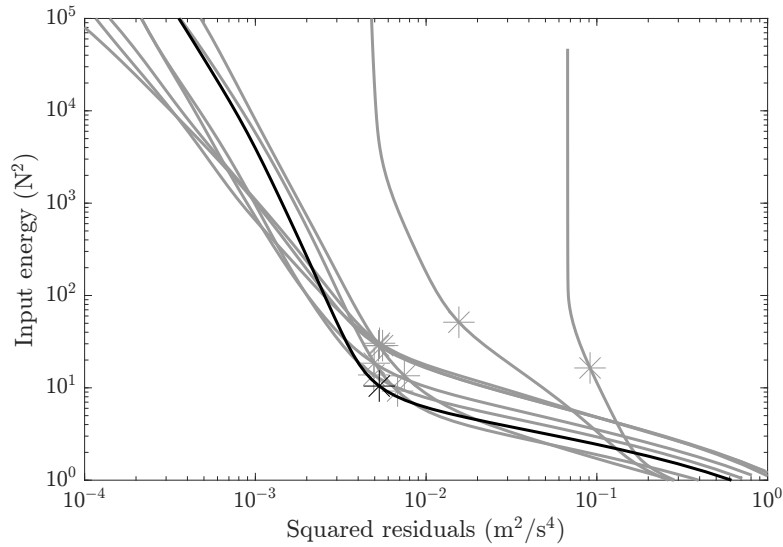


Fig. 5: Demonstration of an intermediate output of the “fixed pivot” method. The ten curves shown are the Pareto optimality curves for the configurations produced by applying the pivoting algorithm to ten values of λ_{fixed} . Then, the joint objective in Eq. (18) is applied to select a curve and input solution, marked in black.

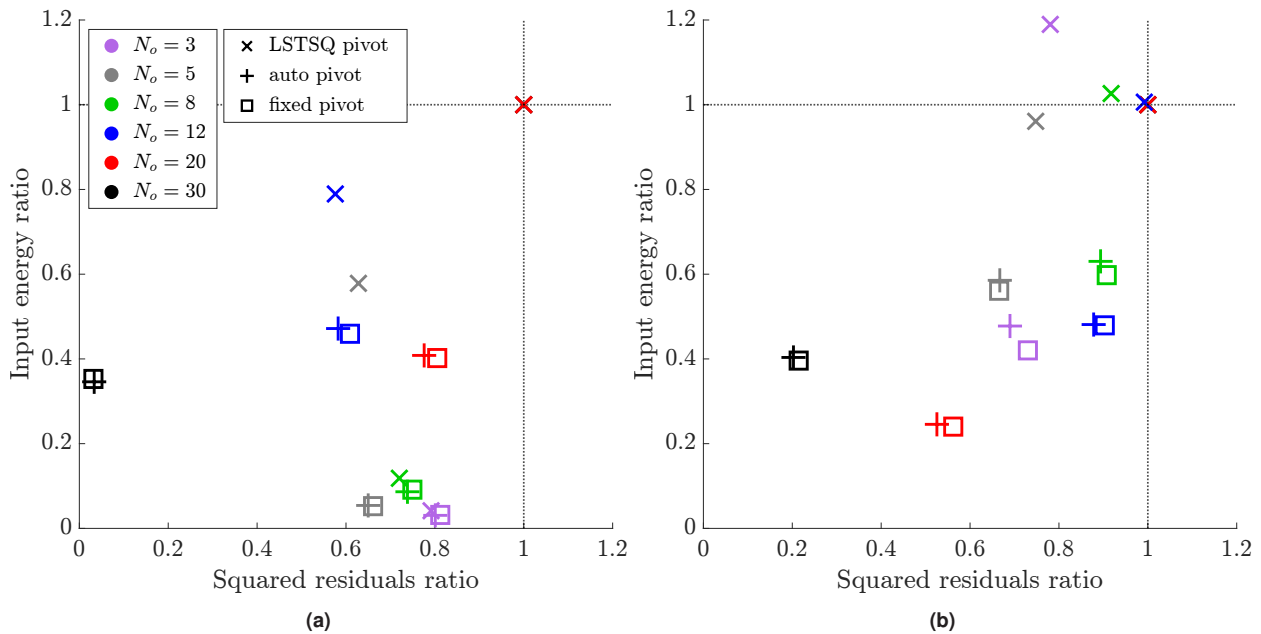


Fig. 6: Performance of experiment design methods for several control channel counts when placing (a) five shakers (b) eight shakers. Squared residuals and inputs are divided by values for the “LSTSQ greedy” method, and the mean ratios over ten trials are shown. Input locations are chosen from 1000 candidate locations. “LSTSQ pivot” is identical for $N_o = 3$ and $N_o = 5$ on both plots.

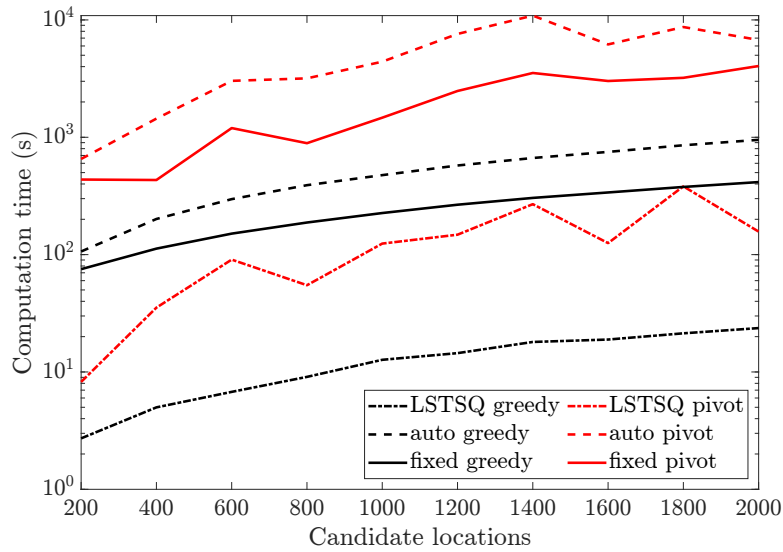


Fig. 7: Computational cost of various methods versus the number of candidate input locations. This example is the placement of six shakers using eight triaxial accelerometers, and “fixed” methods use ten candidate values of λ_{fixed} .

minimization of $g(\lambda)$ does not need to be performed to evaluate each candidate. Based on the similar performance of the two methods, the “fixed pivot” method is recommended when computational cost is a limitation.

5 Conclusion

The major contributions of this paper are summarized as follows. First, an objective function is developed that can be used to place actuators to optimally balance input energy and residuals without any analyst input. Second, an integer programming algorithm is developed to select a set of actuator locations. The algorithm is more computationally expensive than the greedy algorithm, but it is guaranteed to decrease the objective function, yielding generally improved solutions.

The new methods are tested in a simulation with varying numbers of accelerometer measurements and shakers to be placed. Three solution procedures are compared: least squares, direct optimization using the new objective function, and application of the new objective function to a greatly reduced candidate set produced by looping over the regularization parameter. Each of these procedures is solved using the greedy algorithm and the new pivoting algorithm, for a total of six solution methods. The methods are compared by inspecting the Pareto optimality curves for their respective shaker configurations and by direct comparison of the input energy and control accuracy for the full inverse solutions. Pivoting yields better results than the greedy algorithm, and the fully automated and looped parameter methods yield the best results overall. The looped parameter method is recommended in most applications because of its computational efficiency.

Appendix

A Derivation of the regularization parameter selection method

Here we show that $-\ln p(\lambda|\mathbf{Y}) = g(\lambda) + \text{constants}$. Begin with an application of Bayes’ rule with uniform priors,

$$p(\sigma_n, \sigma_x | \mathbf{Y}) \propto \prod_k p(\mathbf{Y}_k | \sigma_n, \sigma_x). \quad (\text{A.1})$$

Note that $\mathbf{Y}_k = \mathbf{H}_k \mathbf{X}_k + \mathbf{E}_k$ with $\mathbf{x}_{jk} \sim \mathcal{N}(\mathbf{0}, \sigma_x \boldsymbol{\Sigma}_x)$ and $\boldsymbol{\varepsilon}_{jk} \sim (\mathbf{0}, \sigma_n \boldsymbol{\Sigma}_n)$ as an error term. Eq. (A.1) can be rewritten as

$$p(\sigma_n, \sigma_x | \mathbf{Y}) \propto \prod_{j,k} \mathcal{N}(\mathbf{y}_{jk} | \mathbf{0}, \sigma_x \mathbf{H}_k \boldsymbol{\Sigma}_x \mathbf{H}_k^H + \sigma_n \boldsymbol{\Sigma}_n). \quad (\text{A.2})$$

A change of variables from σ_n to λ is applied, with $|\partial\sigma_n/\partial\lambda| = \sigma_x$. Then the noise covariance matrix is whitened. Performing these two steps gives

$$p(\lambda, \sigma_x | \mathbf{Y}) \propto \sigma_x \prod_{j,k} \mathcal{N}(\boldsymbol{\Sigma}_n^{-1/2} \mathbf{y}_{jk} | \mathbf{0}, \sigma_x \boldsymbol{\Sigma}_n^{-1/2} \mathbf{H}_k \boldsymbol{\Sigma}_x \mathbf{H}_k^H \boldsymbol{\Sigma}_n^{-1/2} + \sigma_x \lambda \mathbf{I}). \quad (\text{A.3})$$

If $\boldsymbol{\Sigma}_n^{-1/2} \mathbf{H}_k \boldsymbol{\Sigma}_x^{1/2} = \bar{\mathbf{U}}_k \bar{\mathbf{S}}_k \bar{\mathbf{V}}_k^H$, with $\bar{\mathbf{U}}_k^H \bar{\mathbf{U}}_k = \bar{\mathbf{V}}_k^H \bar{\mathbf{V}}_k = \mathbf{I}$, then the distribution above can be rewritten as

$$p(\lambda, \sigma_x | \mathbf{Y}) \propto \sigma_x \prod_{j,k} \mathcal{N}(\bar{\mathbf{U}}_k^H \boldsymbol{\Sigma}_n^{-1/2} \mathbf{y}_{jk} | \mathbf{0}, \sigma_x \mathbf{D}_k + \sigma_x \lambda \mathbf{I}), \quad (\text{A.4})$$

with $\mathbf{D}_k = \bar{\mathbf{S}}_k \bar{\mathbf{S}}_k^H$. The covariance is diagonal, and the normal distributions can be written as the sums of univariate complex normal distributions. Substituting the normal distribution formula and rewriting gives

$$p(\sigma_x, \lambda | \mathbf{Y}) \propto \sigma_x^{1-N_o N_r N_f} \prod_{k,l} (d_{kl} + \lambda)^{-N_r} \exp\left[-\frac{1}{\sigma_x} \sum_{k,l} \frac{-z_{kl}}{d_{kl} + \lambda}\right], \quad (\text{A.5})$$

in terms of quantities in Table 1. Next, the resulting distribution is integrated over σ_x :

$$p(\lambda | \mathbf{Y}) \propto \int_0^\infty p(\sigma_x, \lambda | \mathbf{Y}) d\sigma_x. \quad (\text{A.6})$$

Applying the integral identity

$$\int_0^\infty x^b e^{a/x} dx = (-a)^{1+b} \Gamma(-1-b), \quad b < -1, \quad (\text{A.7})$$

and taking the negative natural logarithm gives $g(\lambda)$ up to an additive constant.

B Efficient minimization of the regularization objective function

Algorithm 3 Efficient minimization of $g(\lambda)$

Initialize a logarithmic grid in the domain of plausible λ , e.g., 200 points between 10^{-10} and 10^{10}
 Initialize d_{kl} and z_{kl} using Table 1
 Compute g for each λ and select λ_0 with the lowest objective
if λ_0 is the first grid point **then**
 Set $\hat{\lambda} = 0$
else
 Perform Newton's method starting at λ_0 . Output $\hat{\lambda}$
end if

Derivatives of $g(\lambda)$ are given by

$$g'(\lambda) = \sum_{k,l} \frac{N_r}{d_{kl} + \lambda} + (2-a) \left(\sum_{k,l} \frac{z_{kl}}{(d_{kl} + \lambda)^2} \right) \left(\sum_{k,l} \frac{z_{kl}}{d_{kl} + \lambda} \right)^{-1}, \quad (\text{B.1})$$

$$g''(\lambda) = - \sum_{k,l} \frac{N_r}{(d_{kl} + \lambda)^2} + (a-2) \left[\left(\sum_{k,l} \frac{z_{kl}}{(d_{kl} + \lambda)^3} \right) \left(\sum_{k,l} \frac{z_{kl}}{d_{kl} + \lambda} \right)^{-1} - \left(\sum_{k,l} \frac{z_{kl}}{(d_{kl} + \lambda)^2} \right)^2 \left(\sum_{k,l} \frac{z_{kl}}{d_{kl} + \lambda} \right)^{-2} \right] \quad (\text{B.2})$$

C Derivation of formulas for accelerated least squares computation

Consider a single frequency line, and define $\mathbf{R}(\mathcal{L}) = \mathbf{Y} - \text{proj}_{\mathbf{H}(\mathcal{L})}\mathbf{Y}$. Here, the projection of a matrix denotes the projections of its columns. We seek to show that $\mathbf{R}(\mathcal{L} \cup c) = \mathbf{R}(\mathcal{L}) - \text{proj}_{\mathbf{N}(c)}\mathbf{R}(\mathcal{L})$, where $\mathbf{N}(c) = \text{proj}_{\text{null}(\mathbf{H}(c))}\mathbf{H}(c)$.

Proof. For conciseness, the notation \mathcal{A}, \mathcal{B} is used to represent subspaces in \mathbb{C}^{N_o} . Begin with the identity

$$\text{proj}_{\mathcal{A} \cup \mathcal{B}}\mathbf{Y} = \text{proj}_{\mathcal{A}}\mathbf{Y} + \text{proj}_{\mathcal{B}}\mathbf{Y} \text{ if } \mathcal{A} \cap \mathcal{B} = \emptyset. \quad (\text{C.1})$$

Because $\mathcal{A} \cup \mathcal{B} = \mathcal{A} \cup (\mathcal{B} \cap \mathcal{A}^c)$,

$$\begin{aligned} \text{proj}_{\mathcal{A} \cup \mathcal{B}}\mathbf{Y} &= \text{proj}_{\mathcal{A}}\mathbf{Y} + \text{proj}_{\mathcal{B} \cap \mathcal{A}^c}(\mathbf{Y} - \text{proj}_{\mathcal{A}}\mathbf{Y}) \\ \iff \mathbf{Y} - \text{proj}_{\mathcal{A} \cup \mathcal{B}}\mathbf{Y} &= (\mathbf{Y} - \text{proj}_{\mathcal{A}}\mathbf{Y}) - \text{proj}_{\mathcal{B} \cap \mathcal{A}^c}(\mathbf{Y} - \text{proj}_{\mathcal{A}}\mathbf{Y}). \end{aligned} \quad (\text{C.2})$$

Taking $\mathcal{A} = \text{col}(\mathbf{H}(\mathcal{L}))$ and $\mathcal{B} = \text{col}(\mathbf{H}(c))$ yields the desired result. \square

Authors' Contributions

Keaton Coletti derived the methods, performed simulation studies, and wrote the manuscript. R. Benjamin Davis and Ryan Schultz advised the project and provided funding. All authors contributed to revising the manuscript.

Acknowledgements

Sandia National Laboratories is a multi-mission laboratory managed and operated by National Technology & Engineering Solutions of Sandia, LLC (NTESS), a wholly owned subsidiary of Honeywell International Inc., for the U.S. Department of Energy's National Nuclear Security Administration (DOE/NNSA) under contract DE-NA0003525. This written work is authored by an employee of NTESS. The employee, not NTESS, owns the right, title and interest in and to the written work and is responsible for its contents. Any subjective views or opinions that might be expressed in the written work do not necessarily represent the views of the U.S. Government. The publisher acknowledges that the U.S. Government retains a non exclusive, paid-up, irrevocable, world-wide license to publish or reproduce the published form of this written work or allow others to do so, for U.S. Government purposes. The DOE will provide public access to results of federally sponsored research in accordance with the DOE Public Access Plan.

References

- [1] P. M. Daborn, C. Roberts, D. J. Ewins, and P. R. Ind. Next-generation random vibration tests. In *Topics in Modal Analysis II*, volume 8, pages 397–410, 2014.
- [2] P. M. Daborn. Scaling up of the impedance-matched multi-axis test (IMMAT) technique. In *Shock & Vibration, Aircraft/Aerospace, Energy Harvesting, Acoustics & Optics*, volume 9, pages 1–10. Springer International Publishing, 2017. doi:10.1007/978-3-319-54735-0_1.
- [3] C. Roberts and D. Ewins. Multi-axis vibration testing of an aerodynamically excited structure. *Journal of Vibration and Control*, 24(2):427–437, 2018. ISSN 1077-5463. doi:10.1177/1077546316642064.
- [4] D. J. Ewins. *Modal Testing: Theory, Practice and Application*. Research Studies Press Ltd., Hertfordshire, England, 2 edition, 2000.
- [5] M. Behling, M. S. Allen, R. L. Mayes, W. J. DeLima, and J. Hower. Influence of shaker limitations on the success of MIMO environment reconstruction. In *Dynamic Environments Testing, Volume 7*, pages 115–129. Springer, Cham, 2023. ISBN 978-3-031-34930-0.
- [6] W. Li, Z. Yang, K. Liu, and W. Wang. MIMO multi-frequency active vibration control for aircraft panel structure using piezoelectric actuators. *International Journal of Structural Stability and Dynamics*, 23(14), 2023. ISSN 0219-4554. doi:10.1142/s0219455423501572.
- [7] N. Niedbal and E. Kusowski. Optimal exciter placement and force vector tuning required for experimental modal analysis. In *Dynamics Specialists Conference*. American Institute of Aeronautics and Astronautics, 1990. doi:10.2514/6.1990-1205.

- [8] D. S. Li, H. N. Li, and C. P. Fritzen. The connection between effective independence and modal kinetic energy methods for sensor placement. *Journal of Sound and Vibration*, 305(4-5):945–955, 2007. ISSN 0022-460X. doi:10.1016/j.jsv.2007.05.004.
- [9] R. Schultz. *Improving Efficiency of Multi-shaker and Combined Shaker-acoustic Vibration Tests*. PhD thesis, University of Massachusetts Lowell, 2019.
- [10] C. Beale, R. Schultz, C. Smith, and T. Walsh. Degree of freedom selection approaches for MIMO vibration test design. In *Special Topics in Structural Dynamics & Experimental Techniques*, volume 5. Springer International Publishing, 2022. doi:10.2172/2001541.
- [11] C. Papadimitriou, J. L. Beck, and S.-K. Au. Entropy-based optimal sensor location for structural model updating. *Journal of Vibration and Control*, 6(5):781–800, 2000. ISSN 1077-5463. doi:10.1177/10775463000600508.
- [12] C. Schumann, M. S. Allen, M. Tuman, W. DeLima, and E. Dodgen. Transmission simulator based MIMO response reconstruction. *Experimental Techniques*, 46(2):287–297, 2022. ISSN 0732-8818. doi:10.1007/s40799-021-00454-4.
- [13] R. Mayes, L. Ankers, P. Daborn, T. Moulder, and P. Ind. Optimization of shaker locations for multiple shaker environmental testing. *Experimental Techniques*, 44(3):283–297, 2020. ISSN 0732-8818. doi:10.1007/s40799-019-00347-7.
- [14] S. Kondoh, C. Yatomi, and K. Inoue. The positioning of sensors and actuators in the vibration control of flexible systems. *JSME international journal. Ser. 3, Vibration, control engineering, engineering for industry*, 33(2):145–152, 1990. ISSN 0914-8825. doi:10.1299/jsmec1988.33.145.
- [15] P. S. Holmes, J. R. Wright, and J. E. Cooper. Optimum exciter placement for normal mode force appropriation using an a priori model. In *Proceedings of IMACXIV, the 14th International Modal Analysis Conference*, 1996.
- [16] D. P. Rohe, G. D. Nelson, and R. A. Schultz. Strategies for shaker placement for impedance-matched multi-axis testing. In *Sensors and Instrumentation, Aircraft/Aerospace, Energy Harvesting & Dynamic Environments Testing, Volume 7*, pages 195–212. Springer International Publishing, 2020. ISBN 978-3-030-12676-6.
- [17] C. Lu, Q. Liu, B. Zhang, and L. Yin. A pareto-based hybrid iterated greedy algorithm for energy-efficient scheduling of distributed hybrid flowshop. *Expert Systems with Applications*, 204:117555, 2022. ISSN 0957-4174. doi:10.1016/j.eswa.2022.117555.
- [18] D. O. Smallwood. Multiple shaker random vibration control - an update. *Sandia National Laboratories SAND98-2044C*, 1999.
- [19] A. Pereira, J. Antoni, and Q. Leclère. Empirical Bayesian regularization of the inverse acoustic problem. *Applied Acoustics*, 97:11–29, 2015. ISSN 0003-682X. doi:10.1016/j.apacoust.2015.03.008.
- [20] R. L. Mayes and D. P. Rohe. Physical vibration simulation of an acoustic environment with six shakers on an industrial structure. In *Shock & Vibration, Aircraft/Aerospace, Energy Harvesting, Acoustics & Optics*, volume 9, pages 29–41. Springer International Publishing, 2017. doi:10.1007/978-3-319-30087-0_4.
- [21] R. Schultz and P. Avitabile. Shape-constrained input estimation for efficient multi-shaker vibration testing. *Experimental Techniques*, 44(4):409–423, 2020. ISSN 0732-8818. doi:10.1007/s40799-020-00361-0.
- [22] R. A. Schultz. A demonstration of force estimation and regularization methods for multi-shaker testing. In *Sensors and Instrumentation, Aircraft/Aerospace, Energy Harvesting & Dynamic Environments Testing*, volume 9, pages 229–243. Springer International Publishing, 2019. doi:10.1007/978-3-030-12676-6_21.
- [23] U. Musella, G. D’Elia, S. Manzato, B. Peeters, P. Guillaume, et al. Analyses of target definition processes for MIMO random vibration control tests. In *Special Topics in Structural Dynamics*, volume 6, pages 135–148. Springer International Publishing, 2017. doi:10.1007/978-3-319-53841-9_12.
- [24] U. Musella, G. D’Elia, A. Carrella, B. Peeters, E. Mucchi, et al. A minimum drives automatic target definition procedure for multi-axis random control testing. *Mechanical Systems and Signal Processing*, 107:452–468, 2018. ISSN 0888-3270. doi:10.1016/j.ymsp.2018.01.039.
- [25] D. O. Smallwood. Multiple-input multiple-output (MIMO) linear systems extreme inputs/outputs. *Shock and Vibration*, 14(2): 107–131, 2007. ISSN 1070-9622. doi:10.1155/2007/701837.
- [26] Y. Ma, H. Chen, and R. Zheng. Control strategy for multi-axial swept sine on random mixed vibration testing. *Journal of Sound and Vibration*, 527:116846, 2022. ISSN 0022-460X. doi:https://doi.org/10.1016/j.jsv.2022.116846.
- [27] R. Schultz and S. Carter. A MIMO time waveform replication control implementation. In *Dynamic Environments Testing*, volume 7, pages 131–140. Springer Nature Switzerland, 2024. doi:10.1007/978-3-031-34930-0_13.

- [28] H. W. Engl and W. Grever. Using the L–curve for determining optimal regularization parameters. *Numerische Mathematik*, 69 (1):25–31, 1994. ISSN 0029-599X. doi:10.1007/s002110050078.
- [29] K.-V. Yuen. *Bayesian Methods for Structural Dynamics and Civil Engineering*. Wiley, 2010. doi:10.1002/9780470824566.
- [30] D. R. Fuhrmann. *Digital Signal Processing Handbook*, chapter Complex Random Variables and Stochastic Processes. CRC Press LLC, 1999.
- [31] R. B. Davis. Spatial correlation function of cylinders in diffuse acoustic fields. *AIAA Journal*, 55(11):4005–4010, 2017. ISSN 0001-1452. doi:10.2514/1.j055805.